Geotextiles and Geomembranes 44 (2016) 799–812

Contents lists available at ScienceDirect

Geotextiles and Geomembranes

journal homepage: www.elsevier.com/locate/geotexmem

Lateral bearing capacity and failure mode of geosynthetic-reinforced soil barriers subject to lateral loadings

Kuo-Hsin Yang [a, *], Jonathan T.H. Wu [b], Rong-Her Chen [c], Yi-Shou Chen [a]

[a] Department of Civil and Construction Engineering, National Taiwan University of Science and Technology, 43, Sec. 4, Keelung Rd., Taipei 106, Taiwan
[b] Department of Civil Engineering, University of Colorado Denver, Denver, CO, USA
[c] Department of Civil Engineering, National Taiwan University, 1, Sec. 4, Roosevelt Rd., Taipei 106, Taiwan

ARTICLE INFO

Article history:
Received 1 December 2015
Received in revised form
5 May 2016
Accepted 30 June 2016
Available online 18 July 2016

Keywords:
Geosynthetics
Reinforced soil structures
Lateral loadings
Finite element
Failure mode

ABSTRACT

In addition to self-weight and vertical surcharge, geosynthetic-reinforced soil (GRS) structures have recently been used as barriers to resist lateral forces from natural disasters, such as floods, tsunamis, rockfalls, debris flows, and avalanches. The stability of such structures subject to lateral loading is often evaluated using conventional external stability analyses with the assumption that the reinforced soil mass is a rigid body. However, this assumption contradicts the flexible nature of reinforced soil. In this study, finite element (FE) models of back-to-back GRS walls were developed to investigate the performance of GRS barriers subject to lateral loading. The FE analysis results indicated that the failure mode and lateral bearing capacity of GRS barriers depend largely on the aspect ratio (L/H: ratio of wall width to wall height). When $0.5 < L/H < 1.0$, the GRS barriers would fail internally because of internal sliding along the soil–reinforcement interface at the loading side and the active soil failure at the opposite side. When $1.0 < L/H < 3.0$, bottom sliding failure would occur along the foundation–reinforcement interface. When $L/H > 3.0$, passive soil failure would occur within the GRS barriers at the side subject to the lateral force. The ultimate lateral bearing capacity of GRS barriers increased with an increase in L/H: the ultimate lateral capacity factor N_L was 1.4–20.1 times K_a for $L/H = 0.5$–3.0. In addition to the effect of L/H, the numerical results indicated that the backfill friction angle ϕ, unit weight γ, and reinforcement vertical spacing S_v considerably affected the lateral bearing capacity of GRS barriers. A hypothetical case study of a GRS barrier against a tsunami force is provided, and a viable method using vertical preloaded soil anchors for improving wall lateral capacity is analyzed and discussed.

1. Introduction

Geosynthetic-reinforced soil (GRS) retaining structures have been widely used in various projects, including buildings, highways, and bridge abutments, to provide improved load bearing behavior. Many past studies focused on the performance and stability of GRS structures subject to vertical loadings (Anubhav and Basudhar, 2011; Ehrlich and Mirmoradi, 2012; Ehrlich et al., 2013; Santos et al., 2013, 2014; Damians et al., 2014; Mirmoradi and Ehrlich, 2014; Cristelo et al., 2016; Nicks et al., 2016). In addition to general applications to carry self-weight and vertical surcharge, GRS structures have recently been used as barriers to resist lateral forces from natural disasters, such as floods, tsunamis, rock falls, debris flows, and avalanches (Brandl, 2011; Fowze et al., 2012; Kuwano et al., 2012; Lambert and Bourrier, 2013; Koseki and Shibuya, 2014), and to protect shorelines (Recio-Molina and Yasuhara, 2005; Yasuhara and Recio-Molina, 2007).

Kuwano et al. (2012) summarized seismic performance of approximately 1600 walls subject to direct impact of the 2011 Tohoku earthquake and tsunami. They observed that more than 90% of the walls did not show any damage. Only less than 1% of the walls were critically damaged because of soil erosion caused by the tsunami. Therefore, multiple tsunami defense facilities using GRS structures (Fig. 1) were proposed by the Japanese Geotechnical Society (JGS, 2011) after the 2011 Tohoku earthquake. Yasuhara and Recio-Molina (2007) conducted a series of model tests on geotextile wrap-around revetments (GWRs) against wave action. The GWRs were stable against the wave action, and their stability can be further increased with a few simple modifications (i.e., GWRs with

* Corresponding author. Fax: +886 2 2737 6606.
E-mail addresses: khy@mail.ntust.edu.tw (K.-H. Yang), Jonathan.Wu@ucdenver.edu (J.T.H. Wu), rongherchen@ntu.edu.tw (R.-H. Chen), ericchin21020@hotmail.com (Y.-S. Chen).

http://dx.doi.org/10.1016/j.geotexmem.2016.06.014
0266-1144/

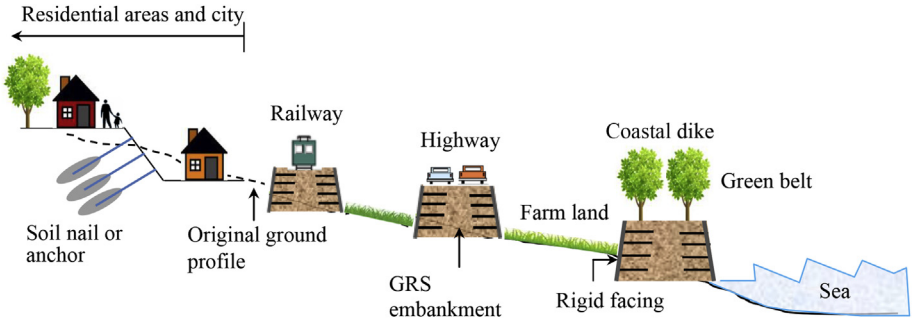

Fig. 1. Multiple tsunami defense facilities using GRS structures proposed by the Japanese Geotechnical Society after the 311 Great East Japan Earthquake in 2011 (replotted from JGS, 2011).

a seaward face are injected with mortar, and the reinforcement layers are sewn together). Moreover, their tests demonstrated that GWRs performed favorably against differential settlement and scour erosion.

Ronco et al. (2009) and Peila et al. (2007) performed several full-scale tests and finite element (FE) dynamic modeling of reinforced embankments for rockfall protection. Embankments made of various geogrid types, soils, and construction layouts were tested at various impact energy levels to evaluate the resistance impact of these structures. They concluded that among various protection methods, reinforced embankments can be considered an effective technique. Walz (1982) conducted 20 dynamic 1 g model tests on protective barriers against rockfalls (reported by Brandl, 2011). The GRS barriers effectively absorbed the impact energy from rockfalls. Lambert and Bourrier (2013) provided a comprehensive review of rockfall protection by using GRS embankments. In Taiwan, many GRS embankments have been constructed as debris and rockfall barriers (Fig. 2). In addition to lateral loadings induced by nature, impact of lateral loadings from blasts on reinforced soil (Tuan, 2013) and impact of traffic on reinforced structures (Soude et al., 2013; Kim et al., 2010) have been investigated.

Earthquake-induced seismic loading is another type of lateral loading on GRS structures. The performance of GRS structures under seismic loadings has been extensively investigated, and these studies have reported satisfactory performance of GRS structures against seismic loadings (e.g., Tatsuoka et al., 1995; Bathrust and Hatami, 1998; Matsuo et al., 1998; El-Emam and Bathurst, 2004, 2005, 2007; Ling et al., 2005; Nova-Roessig and Sitar, 2006; Krishna and Latha, 2007; Latha and Krishna, 2008; Liu et al., 2010; Huang et al., 2010, 2011; Murali and Madhavi, 2012; Vahedifard et al., 2013; Ren et al., 2016). The seismic design methods in design guidelines (Berg et al., 2009; Elias et al., 2001) typically assume seismic loading to be an inertial force that acts laterally on the centroid of the failure mass of reinforced soil to assess seismic internal stability, and use the pseudostatic Mononobe–Okabe method to calculate the dynamic earth pressure to evaluate seismic external stability. Notably, GRS structures directly subject to lateral impacts from natural disasters may respond differently to those

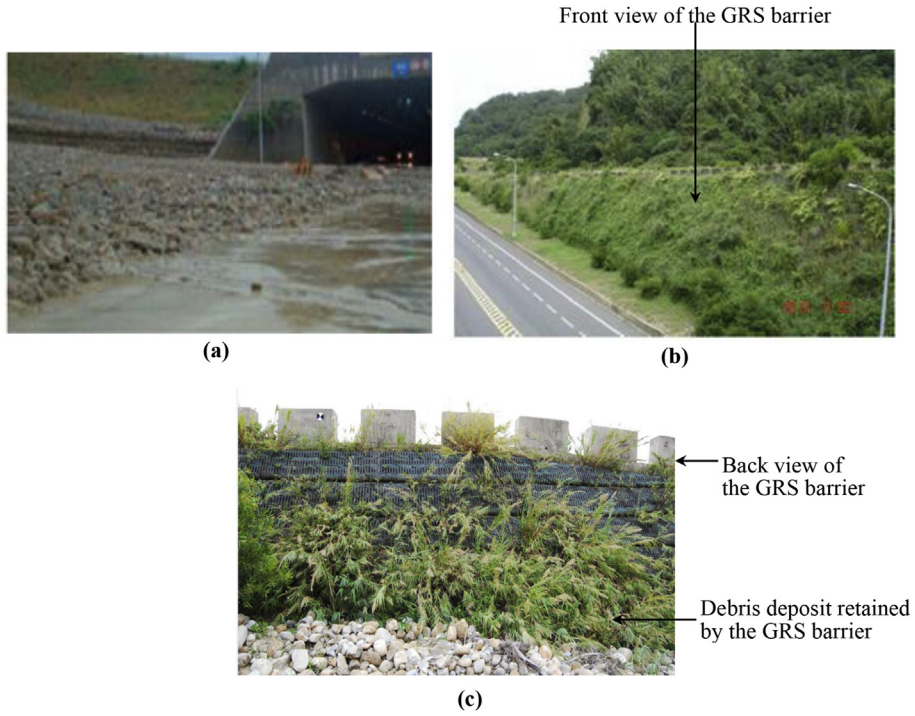

Fig. 2. Application of GRS structures against debris flow in mountain area in Taiwan: (a) debris deposited on the local road (Tai 140 Line) before construction of a GRS barrier; (b) front view; and (C) back view of a GRS embankment (wrapped around facings) as a debris barrier.

under seismic loadings. However, in contrast to seismic studies, studies on performance and stability of GRS structures subject to lateral loadings are relatively limited.

Design of GRS walls against various external modes of failure (i.e., sliding and overturning failures) has been addressed in GRS structure design guidelines (e.g., Berg et al., 2009; Elias et al., 2001) by considering active earth pressure from retained soils that acts laterally on the GRS walls. Some studies (Choudhury and Ahmad, 2007; Yasuhara and Recio-Molina, 2007) have adopted a similar force and moment equilibrium approach to assess the stability of GRS retaining structures subject to lateral loadings. In these approaches, the reinforced soil mass is treated as a rigid body, which is independent of soil and reinforcement strength properties. However, this assumption contradicts the *flexible* nature of reinforced soil and likely cannot accurately describe the behavior and failure mode of GSR structures subject to lateral loadings. In addition, sophisticated methods have been proposed to investigate the kinematic energy and dynamic impacts of rockfalls (Brandl, 2011; Ronco et al., 2009; Peila et al., 2007).

This study aimed to (1) develop a FE model for GRS walls with back-to-back configuration and (2) investigate the failure mode and lateral bearing capacity of GRS barriers subject to lateral loadings. First, a back-to-back GRS wall model was developed and verified using experimental results of a large-scale test on a GRS wall. Previous studies have analyzed GRS walls with a typical configuration (i.e., with retained soil behind a wall) by using numerical and physical measures. However, GRS walls with back-to-back configurations have not been thoroughly studied, especially for applications as barriers. Han and Leshchinsky (2010) analyzed the behavior of back-to-back reinforced walls by using FLAC (finite difference) and ReSSA (limit equilibrium) software. They investigated the effect of aspect ratio L/H (ratio of wall width to wall height) on internal and external stabilities of reinforced walls under self-weight conditions. However, vertical surcharge and lateral loads were not considered. In this study, the reinforced soil was treated as a deformable continuum instead of a rigid body; therefore, the true failure mode was described. Second, numerical simulations of GRS barriers subject to lateral loadings with various L/H values were performed. The failure mode and calculated ultimate lateral capacity are discussed. Third, a parametric study was conducted to identify the factors (i.e., soil and reinforcement properties, and wall geometry) with the most significant influences on the ultimate lateral capacity of GRS barriers. Finally, a hypothetical case study of a GRS barrier against tsunami force is illustrated, and an improved method for resisting lateral forces of GRS barriers is discussed. The results of this study should provide insightful information on the behavior and design of GRS structures subject to lateral loadings.

2. Numerical model and verification

An FE model of a back-to-back GRS wall was developed and verified using a large-scale soil-geosynthetic composite (SGC) test (Wu et al., 2014, 2011; Wu and Pham, 2013). The SGC Test 4 was selected. The wall was 2 m high, 1.4 m wide ($L/H = 0.7$), and had reinforcement spacing $S_v = 0.4$ m (Fig. 3). The backfill was diabase-crushed gravel with a maximum particle size of 33 mm, classified as well-graded gravel (GW) according to the Unified Soil Classification System. Large-size triaxial test (specimen diameter = 150 mm; height = 300 mm) results indicated that the backfill had a peak friction angle $\phi' = 50^\circ$ and cohesion $c' = 76.6$ in the stress range of interest. The reinforcement was a polypropylene (PP) woven geotextile with an ultimate tensile strength $T_{ult} = 70$ kN/m and stiffness $J = 700$ kN/m obtained from a wide width tensile test (ASTM D4595). The backfill was placed and compacted to 98% of maximum dry density in 0.2-m. Hollow concrete blocks (397 mm × 194 mm × 194 mm) were used as formworks for construction during specimen preparation. However, they were removed before loading. The entire surface area of the test specimen was sealed with a 0.5-mm-thick latex membrane, and a confining pressure of 34 kPa was applied to the GRS wall by vacuuming. A hydraulic jack was rested on a 30-cm-thick concrete pad, which was placed on top of the specimen, and the GRS wall was then loaded gradually until failure occurred. The maximum applied vertical pressure was approximately 1300 kPa. Wall vertical and lateral movements were measured using several linear variable differential transformers (LVDTs) and digital dial indicators, which were uniformly distributed on wall top and two sides.

The FE program PLAXIS v8.2 (PLAXIS, 2005) was selected for the analysis. The soil was simulated using a hardening soil (hyperbolically elastoplastic) model. The input soil parameter values were calibrated using the stress–strain–volumetric data obtained from the aforementioned large-size triaxial tests. The reinforcement was simulated using a linearly elastic perfectly plastic model. Because tensile strength properties of the geotextile are influenced by the applied strain rate (10%/min in the wide-width tensile test is considerably higher than that developed in the test wall), reduction factors of 0.77 and 0.67, deduced from Boyle et al. (1996), were applied to the ultimate tensile strength and stiffness of reinforcement, respectively. Consequently, $T_{ult} = 54$ kN/m and $J = 470$ kN/m were input in the reinforcement model in the FE simulation. The soil–reinforcement interaction was modeled, and a reduction (or efficiency) factor of $R_{inter} = 0.8$ was applied to the soil material. The facing blocks were modeled as a concrete material. Block–block and block–soil interfaces were not considered in the model because the facing block was a temporary structure required for construction during specimen preparation and was deactivated before surcharging. Table 1 presents the material and geometric parameters of the validation.

The FE analysis was conducted by following the construction procedure (i.e., staged construction and compaction) for preparation of the SGC specimen. Compaction of each soil lift was simulated by applying a uniform equivalent compaction pressure of 44 kPa on top of the newly placed soil layer before the model acquired equilibrium, and removed the applied compaction pressure before placing the next soil lift. The compaction pressure of 44 kPa was obtained from the actual plate compactor used in the SGC tests. A similar numerical procedure was adopted by Hatami and Bathurst (2005) and Guler et al. (2007) using compaction pressure of 8 kPa to modeling compaction. An additional sensitivity study was conducted to evaluate the effect of compaction pressure. Although the applied compaction pressure value differs from the one (i.e., 8 kPa) used in Hatami and Bathurst (2005) and Guler et al. (2007), the results of the sensitivity study revealed that the magnitude of compaction pressure has little effect on the wall behavior (e.g., wall deformation and reinforcement strain) because the compaction-induced wall facing deformation was constrained by the rigid concrete facing blocks in the wall model. At the end of construction, the facing blocks were deactivated, and a uniform surcharge was subsequently applied on top of the FE model with a load increment of 200 kPa until wall failure occurred. Fixed boundary conditions in both the horizontal and vertical directions were employed at the wall bottom. The applied fixed boundary conditions can be justified by nearly no lateral displacement observed at the wall bottom because of the high friction resistance from the concrete floor slab.

Failure patterns, lateral displacement, and global stress–strain relationships, obtained using the FE analyses, and test results are shown in Figs. 4 and 5. The global vertical strain in Fig. 5b was calculated using the average vertical deformation, which was

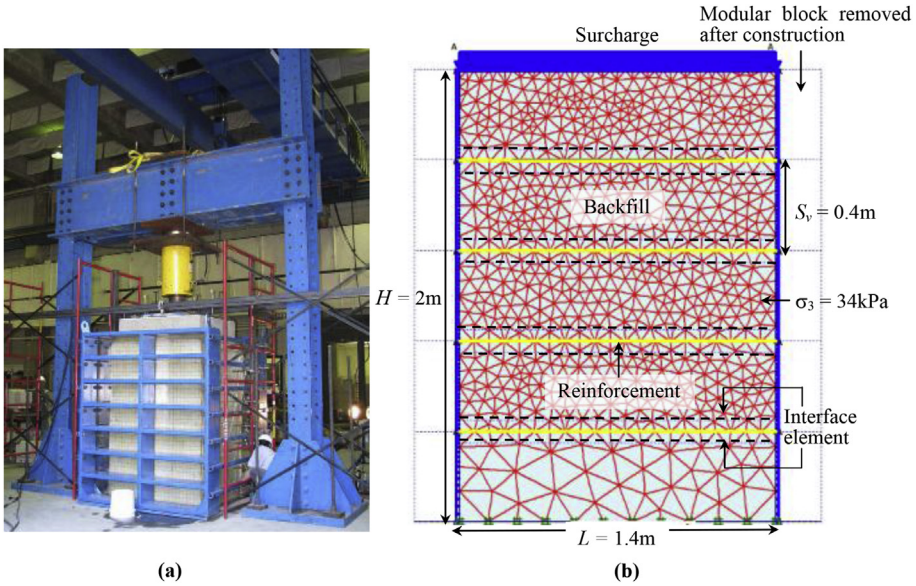

Fig. 3. The large-scale GRS wall: (a) physical model; (b) FE mesh and dimensions.

measured by LVDT and digital dial indicators, divided by the original wall height (=2 m). Fig. 4 shows similar crossing shear planes obtained using numerical simulation and physical test. Fig. 5 shows a satisfactory agreement between the measured and calculated values of lateral displacement and global stress–strain relationships in all loading stages. Numerical illness occurred at a surcharge level close to the peak applied surcharge of the physical test. In summary, FE results were consistent with the measured data, demonstrating validity of the FE model for simulation of back-to back GRS structures.

3. Failure mode study

3.1. FE model

The validated FE model was used to study the failure mode and lateral bearing capacity of GRS barriers subject to lateral loadings. Table 1 presents the material parameters in the failure mode study. Different from the validation study, the input soil unit weight, soil shear strength properties, and wall height were modified to represent general GRS wall cases. A wrap-around facing was

Table 1
Material and geometric parameters in the FE simulation.

Property	Value	
	FE validation	Failure mode study (baseline case)
Backfill (Hardening Soil)		
γ, unit weight (kN/m^3)	24	20
E_{50}^{ref}, secant modulus (kPa)	80,000	80,000
E_{oed}^{ref}, tangent oedometer loading modulus (kPa)	60,000	60,000
E_{ur}^{ref}, unloading-reloading modulus (kPa)	160,000	160,000
ν_{ur}, unloading-reloading Poisson's ratio	0.2	0.2
m, modulus exponent	0.5	0.5
R_f, failure ratio	0.9	0.9
ϕ', friction angle (degree)	50	40
c', cohesion (kPa)	76.6	2
ψ, angel of dilatancy (degree)	15	15
R_{inter}, interface factor	0.8	0.8
Reinforcement (Linear elastic-perfectly plastic)		
J, stiffness (kN/m)	470	470
T_{ult}, ultimate tensile strength (kN/m)	54	54
Facing Block (Linear elastic)[a]		
γ, unit weight (kN/m^3)	12.5	12.5
E, Young's modulus (kPa)	3,000,000	3,000,000
ν, Poisson's ratio	0.15	0.15
Geometric configuration		
H, wall height (m)	2	3
L/H, wall aspect ratio	0.7	0.7
S_v, reinforcement vertical spacing (m)	0.4	0.4
Applied load type	Uniformly vertical	Linearly lateral

Note:
[a] Facing blocks were deactivated at the end of construction.

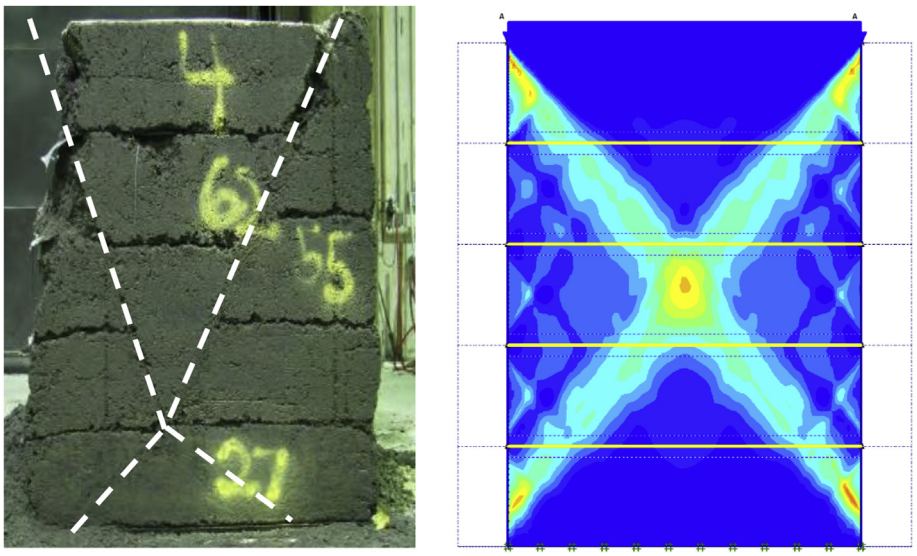

Fig. 4. Failure pattern: (a) GRS specimen after test; (b) FE result of incremental shear strain.

modeled by connecting the geogrid elements in PLAXIS around the facing and was extended into the reinforced soil zone with an overlap length of 0.2 *L*. The soil–reinforcement interface, a crucial factor that captures interlayer sliding within GRS barriers, was modeled. The effect of the foundation stiffness was not considered; a firm foundation was modeled. The foundation–reinforcement interface was considered by placing a 1-cm thin soil layer between the bottommost reinforcement layer and foundation. Consistent with the reduction factor R_{inter} = 0.8 used for the soil–reinforcement interfaces in this mode, 80% of the backfill shear strength and stiffness properties were used for the thin soil layer. This approach allowed the GRS barrier model to fail along the foundation–reinforcement interface (i.e., bottom sliding failure) when the resisting strength was reached. However, bearing capacity failure was not permitted. After wall construction was completed, a linear lateral pressure was applied to the GRS barrier model and was gradually increased until the wall failed. Mesh updating was used to model large deformations.

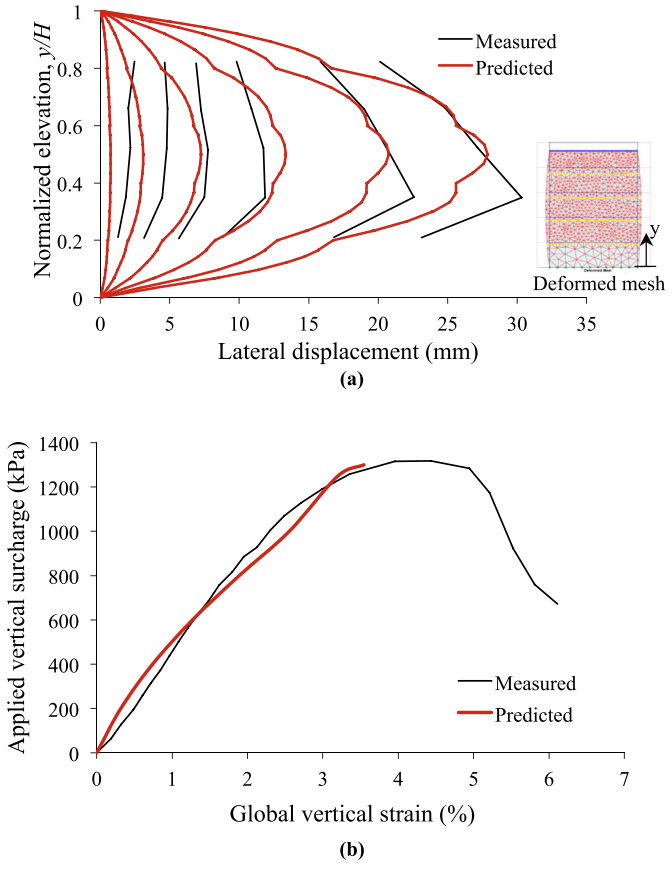

Fig. 5. Comparison of predicted and measured results: (a) lateral displacement under each 200 kPa surcharge increment; (b) applied vertical stress vs. global vertical strain.

3.2. Failure mode of GRS barrier with *L*/*H* = 0.7

Fig. 6 shows the predicted lateral load–displacement curve of a GRS barrier with *L*/*H* = 0.7, regarded as the baseline case. The FE results indicated that the maximum lateral displacement occurred

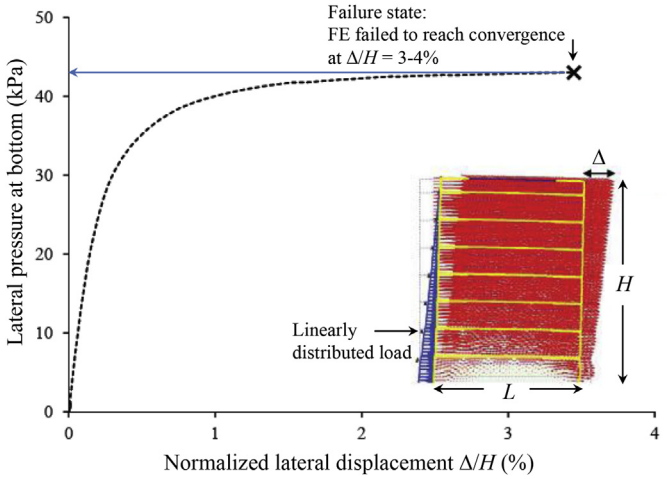

Fig. 6. Predicted load–displacement curve for the GRS barrier (*L*/*H* = 0.7 baseline case).

at top of the wall and decreased linearly with the depth. The lateral displacement increased with increasing lateral load. When the applied lateral pressure at the bottom reached 43 kPa, the wall failed at a normalized lateral displacement, Δ/H, of approximately 3%–4%. The ultimate lateral capacity of GRS barrier was determined at the failure state (Fig. 6). The corresponding total lateral resistance is $P_u = 64.5$ kN/m. The dimensionless ultimate lateral capacity factor is $N_L = 0.71$, which is defined as

$$N_L = \frac{P_u}{1/2\gamma H^2} = \frac{\sigma_{h@bottom}}{\gamma H} \quad (1)$$

where P_u is the total lateral resistance per unit length, γ is the unit weight of backfill, H is the wall height, and $\sigma_{h@bottom}$ is the applied ultimate lateral pressure at the bottom. The N_L is the ratio of the maximum lateral pressure at the bottom to the corresponding soil overburden pressure. One can regard N_L an equivalent lateral pressure coefficient required for a failure of GRS barrier.

Fig. 7 shows the development of Mohr–Coulomb failure points within the GRS barrier. The failure mode is internal sliding along the soil–reinforcement interfaces at the lower half part of the GRS barrier on the side where loading is applied (referred to as the loading side) and is an active failure of the reinforced soil on the other side where no external loads were applied (referred to as free-end side). Stress distribution along the horizontal direction was examined; the numerical results revealed that as lateral loadings increased, the vertical stress decreased in the left part of the GRS barrier, and the vertical stress increased in the right part of the GRS barrier.

Fig. 8a shows the distribution of vertical stress increment (with respect to the vertical stress at the end of construction) caused by an applied lateral pressure of 30 kPa at the bottom along the horizontal direction. A negative vertical stress increment ($\Delta\sigma_v < 0$) was observed in the left part of the GRS barrier (toward the loading side), and a positive vertical stress increment ($\Delta\sigma_v > 0$) was observed in the right part of the GRS barrier. This stress distribution is similar to a cantilever-type bending (or flexural) stress (Fig. 8b). For comparison, the bending stress calculated using theoretical elastic flexure formulas is plotted (Fig. 8a) and is expressed as

$$\Delta\sigma_v = \frac{Mx_1}{I} \quad (2)$$

where M is the lateral loading-induced bending moment, x_1 is the horizontal distance from the neutral plane (positive when toward the right), and I ($=L^3 \times 1/12$) is the moment of inertia of the cross-section of the GRS barrier. The bending stress calculated using Eq. (2) matched reasonably with the $\Delta\sigma_v$ obtained from FE simulation. The discrepancy was attributable to the change of the cross-section dimension of the GRS barrier by mesh updating function.

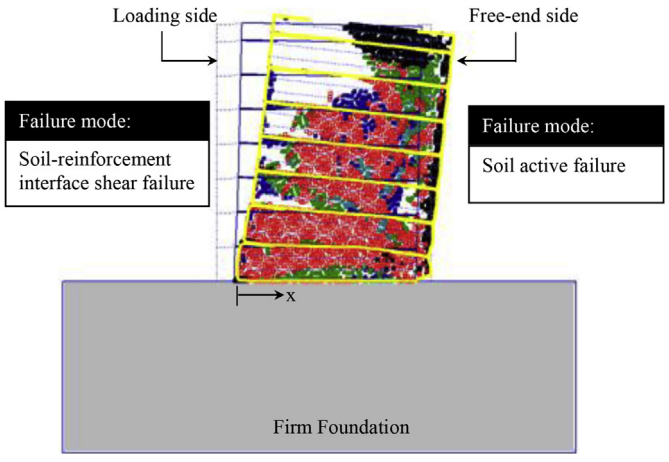

Fig. 7. Failure mode and development of Mohr-Coulomb failure points in the GRS barrier ($L/H = 0.7$ baseline case).

In the loading side of the GRS barrier, the negative $\Delta\sigma_v$ caused a reduction in normal stress along the soil–reinforcement interface, resulting in interface slippage between soil and reinforcement. This has been demonstrated by the development of Mohr–Coulomb failure points along the second to fourth reinforcement layers (Fig. 7). Interface slippage can be readily observed in the interface shear stress information. Fig. 9 shows completely mobilized soil–reinforcement interface shear strength along the wall width from the loading side. The definition of interface shear stress mobilization ratio in Fig. 9 is given as

$$\tau_{rel} = \frac{\tau_{mobilized}}{\tau_{\max}} \quad (3)$$

where $\tau_{mobilized}$ is mobilized shear stress along the soil–reinforcement interface, τ_{max} is maximum interface shear strength. This failure mechanism is consistent with previously reported numerical simulations (Carotti et al., 2000; Ronco et al., 2009). They observed several shear planes along the reinforcement layers within GRS embankments subject to impact force from rockfalls. They indicated that although reinforcement layers could enhance the performance of embankments to withstand the rock impact, horizontal planar reinforcement layers may offer a preferential plane for interface shear failure.

Several active failure planes were evident in the free-end side of the GRS barrier (Fig. 7). These active failures were induced by an increase in the vertical stress ($\Delta\sigma_v > 0$) that resulted from an increase in the applied lateral pressure. Because of the effect of the applied lateral pressure, the active failure induced by the vertical stress increment is similar to that of GRS walls subject to vertical surcharge in conventional applications.

Fig. 10 shows the mobilized reinforcement tension force along each reinforcement layer at different loading stages. Little reinforcement tensile force was mobilized at the end of construction because of the effect of compaction and soil self-weight. The maximum tensile force of reinforcement was approximately located at the middle of each reinforcement layer because of the symmetric loading conditions during construction. In the failure state, the mobilized reinforcement tensile force markedly increased on the loading side of the GRS barrier, particularly in reinforcement layers 1–4. The increase in the mobilized reinforcement tensile force can be attributed to the active soil failure caused by an increase in the vertical stress at this side. The mobilized reinforcement tensile force had a negligible difference in the opposite side because of the interface slippage on the free-end side of the GRS barrier. In summary, the numerical results suggest that the failure modes of a GRS barrier with $L/H = 0.7$ are internal. Reinforcement can contribute to the internal stability by soil–reinforcement interaction and mobilized reinforcement tensile loads at loading and free-end sides of the GRS barrier, respectively. The internal failure mode obtained using numerical simulation differed from that of a rigid body assumed for reinforced soil mass in design guidelines.

3.3. Failure mode with different L/H ratios

The FE results indicated that the failure mode changed with a change in L/H. The $\Delta\sigma_v$ induced by the applied lateral loads decreased with an increase in the wall width because the moment of inertia of GRS barriers increased with increasing wall width (see

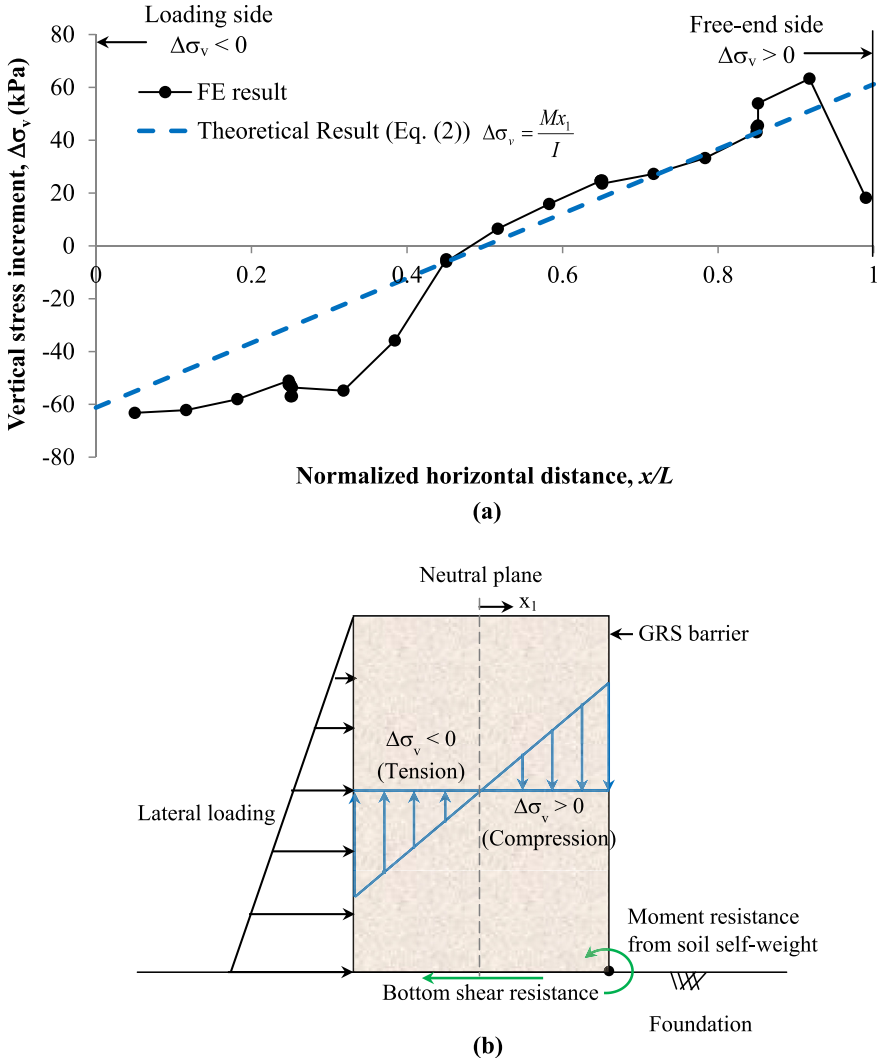

Fig. 8. Development of bending stress inside the GRS barrier: (a) distribution of vertical stress increment along horizontal direction due to the applied lateral pressure of 30 kPa at bottom; (b) schematic illustration of cantilever-type bending stress.

Eq. (2)). Consequently, a GRS barrier with a high *L*/*H* ratio did not fail because of the same failure mechanism as discussed previously for the GRS barrier with *L*.*H* = 0.7. Fig. 11 shows the development of Mohr–Coulomb failure points with different *L*/*H* ratios. When *L*/*H* = 2.2 (Fig. 11a), the prevailing failure mode was sliding at the wall bottom because of failure along the foundation–reinforcement interface. When *L*/*H* = 4.2 (Fig. 11b), the bottom frictional resistance increased so that bottom sliding did not occur. Instead, a passive soil failure governed the failure mode of the GRS barrier with a high *L*/*H* ratio. A clear passive failure surface was observed from the Mohr–Coulomb failure points (Fig. 11b).

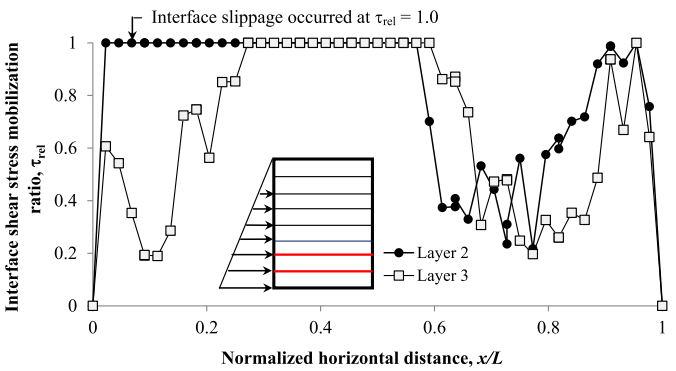

Fig. 9. Distribution of the mobilized interface shear stress along the second and third soil-reinforcement interfaces.

4. Ultimate lateral bearing capacity

Fig. 12 shows the variation of the ultimate lateral capacity factor N_L with a change of *L*/*H*. The N_L is a dimensionless factor as defined in Eq. (1). The values calculated using normalized theoretical overturning and sliding equations were plotted for comparisons. The normalized theoretical overturning and sliding equations are presented in Eqs. (4-2) and (5-2), respectively, and are derived as follows:

For overturning failure based on moment equilibrium,

$$P_u \times \frac{H}{3} = W \times \frac{L}{2} \tag{4}$$

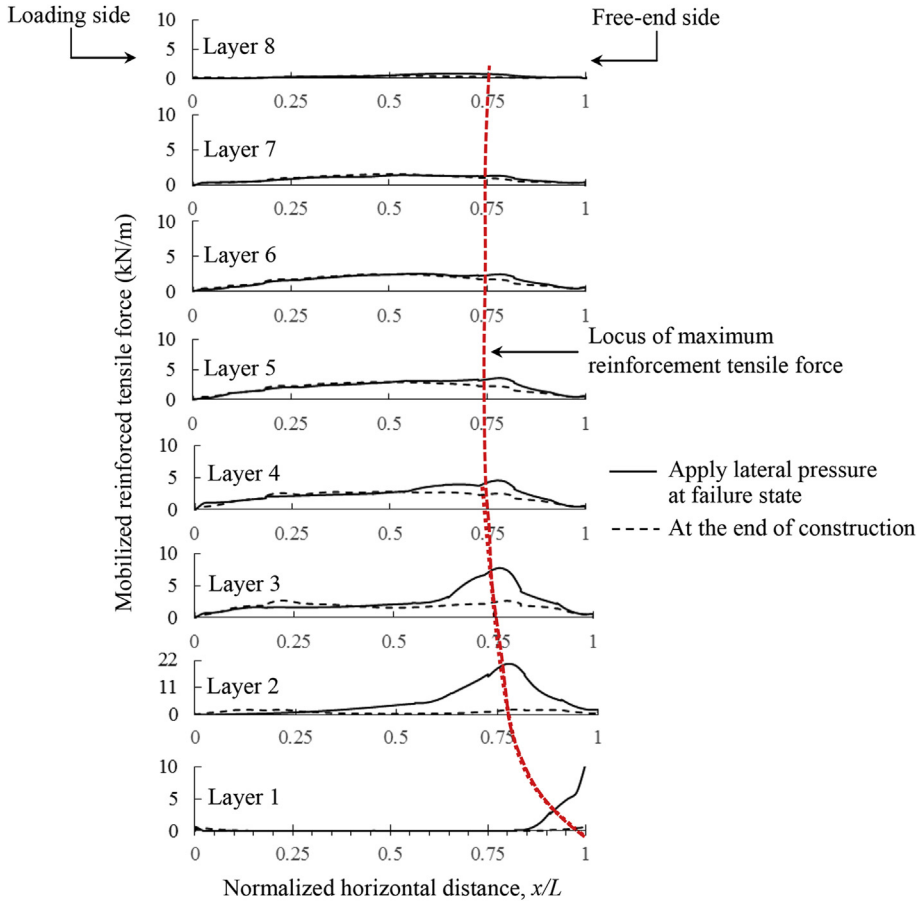

Fig. 10. Mobilized reinforcement tensile force within the GRS barrier ($L/H = 0.7$ baseline case) at the end of construction and at failure state.

$$\left(\sigma_{h@bottom} \times \frac{H}{2}\right) \times \frac{H}{3} = (\gamma HL) \times \frac{L}{2} \tag{4-1}$$

$$N_L = \frac{\sigma_{h@bottom}}{\gamma H} = 3 \times \left(\frac{L}{H}\right)^2 \tag{4-2}$$

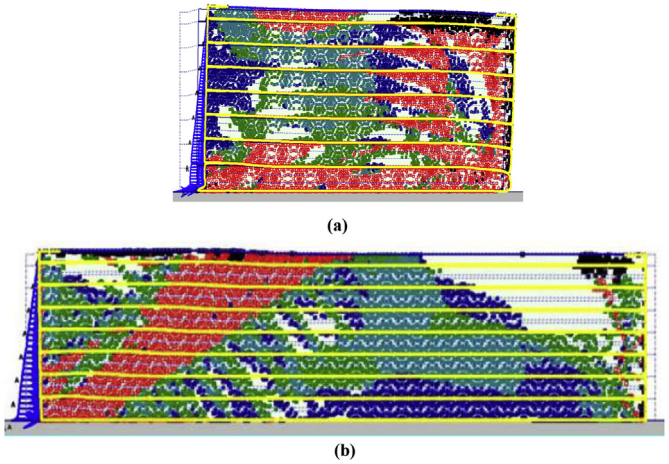

Fig. 11. Development of Mohr-Coulomb failure points (red color): (a) interface sliding failure at bottom for $L/H = 2.2$. (b) soil passive failure for $L/H = 4.2$. (For interpretation of the references to colour in this figure legend, the reader is referred to the web version of this article.)

For sliding failure based on horizontal force equilibrium,

$$P_u = W \times \tan\delta + L \times c_a \tag{5}$$

$$\sigma_{h@bottom} \times \frac{H}{2} = \gamma HL \times \left(\tan\delta + \frac{c_a}{\gamma H}\right) \tag{5-1}$$

$$N_L = \frac{\sigma_{h@bottom}}{\gamma H} = \frac{2L}{H} \times \left(\tan\delta + \frac{c_a}{\gamma H}\right) \tag{5-2}$$

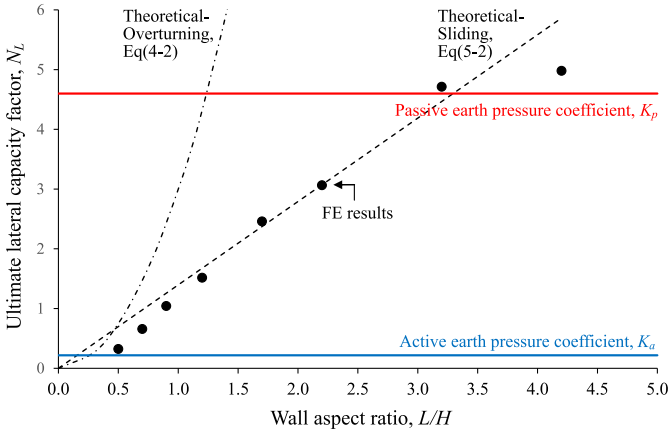

Fig. 12. Ultimate lateral capacity factor versus wall aspect ratio.

where W is self-weight of the GRS barrier per unit length and δ and c_a are reinforcement–foundation interface friction angle and adhesion, respectively. Corresponding to the input values in the FE analyses, 80% of the backfill shear strength was assigned to δ and c_a. The other parameters were as defined previously.

Fig. 12 shows N_L increased with an increase in L/H, indicating that the ultimate lateral bearing capacity of the GRS barrier increased with an increase in the wall width. Table 2 summarizes the ultimate lateral capacity factors and the corresponding failure modes with various L/H ratios. When $0.5 < L/H < 1.0$, N_L was greater than Rankine's theoretical active earth pressure coefficient K_a. However, it was lower than the values calculated using normalized theoretical overturning and sliding equations. The result of $N_L > K_a$ indicated that a GRS wall with L/H in this range can withstand an active lateral earth pressure, which is a common example of a GRS wall resisting active lateral earth pressure from retained fill or natural slopes. In this L/H range, the N_L was 1.4–5.5 times the K_a (Table 2), suggesting that the GRS barrier with $0.5 < L/H < 1.0$ can laterally bear 1.4–5.5 times the active lateral earth pressure. The result of N_L lower than the values calculated using theoretical overturning and sliding equations suggests that a GRS wall in this L/H range will fail internally before the external failure occurs, which can explain why overturning failure of GRS walls has not been observed in the field. The internal soil failure obtained using FE method differed from that in conventional external stability analyses in which the reinforced soil mass is assumed to be a rigid body. This assumption contradicts the flexible nature of reinforced soil; consequently, the conventional analyses cannot accurately predict the ultimate lateral bearing capacity of GRS barriers.

When $1.0 < L/H < 3.0$, N_L followed the theoretical sliding equation, suggesting that the dominant failure mode was a sliding failure along the wall base. The numerical agreement between the FE and theoretical results supported the observed foundation–reinforcement interface failure of the GRS barrier with $L/H = 2.2$ (Fig. 11a). In this L/H range, the N_L was 5.5–20.1 times the K_a. When $L/H > 3.0$, the N_L reached the Rankine's passive lateral earth pressure coefficient K_p. A clear passive failure surface was observed for the GRS barrier with $L/H = 4.2$ (Fig. 11b). Fig. 12 shows that the N_L value is slightly higher than the theoretical K_p value at $L/H = 4.2$. This is because a small amount of cohesion input in the soil model in the FE analyses was not included in the Rankine's equation for calculating K_p. Because the passive failure is a function of the soil shear strength, a further increase in L/H did not improve the ultimate lateral bearing capacity of a GRS barrier. Notably, the L/H values for different failure modes discussed in this section and listed in Table 2 are only applicable for the GRS walls with the similar backfill used in this paper (i.e., $\phi' = 45°$). The L/H values may be subject to change depending on the friction angle of the backfill.

5. Parametric study

Parametric analyses were conducted to examine quantitative influence of wall configurations, and soil and reinforcement properties on lateral bearing capacity of GRS barriers. The parameters investigated were wall aspect ratio L/H, soil unit weight γ, soil friction angle ϕ, soil modulus E_{50}^{ref}, interface reduction factor R_{inter}, reinforcement stiffness J, ultimate tensile strength T_{ult}, and vertical spacing S_v. Table 3 provides a summary of input parameter values in the parametric study. Only one target parameter was varied each time and others were remained unchanged in the parametric study.

Fig. 13a and d present the load–displacement curves for GRS barriers with various values of ϕ, E_{50}^{ref}, L/H, and S_v, respectively. The internal soil failure predicted by the FE analyses suggested that the soil shear strength played a crucial role in lateral bearing capacity of the GRS barriers. As demonstrated in Fig. 13a, the lateral bearing capacity increased with an increase in ϕ. The numerical results demonstrated again that the shear strength-dependent internal soil failure differed from that obtained using the conventional external stability analyses in which the reinforced soil mass is assumed to be a rigid body. Fig. 13b shows that the load–displacement curve became stiffer with an increase in E_{50}^{ref}. However, E_{50}^{ref} appeared to have a minor effect on ultimate lateral bearing capacity of the GRS barrier. Fig. 13c shows that the lateral bearing capacity significantly increased with an increase in L/H. As discussed previously, both negative and positive values of vertical stress increment $\Delta\sigma_v$ become smaller with increasing wall width, leading to a higher normal pressure (stronger soil–reinforcement interaction) on the loading side and a lower vertical stress (a stable state of soil) on the free-end side. Fig. 13d shows that the lateral bearing capacity increased with a reduction in S_v. By examining the stress information, a higher lateral stress was found to develop at smaller S_v. The reinforcement-induced lateral stress served as an additional confining pressure to increase the soil shear strength and therefore enhance the lateral bearing capacity of the GRS barrier. The increase in the lateral stress with the reduction in S_v was also observed by Hong and Wu (2013) for reinforced sand columns.

Fig. 14 shows an overall result of the parametric study, which is presented as change in ultimate lateral resistance (%) versus change in the input parameter (%). The results indicated that the aspect ratio L/H, backfill friction angle ϕ, unit weight γ, and reinforcement vertical spacing S_v had considerable influences on lateral bearing

Table 3
Summary of input parameters in the parametric study.

Property	Value		
	Decreased	Baseline	Increased
Backfill			
γ, unit weight (kN/m^3)	15	20	25
E_{50}^{ref}, secant modulus (kPa)[a]	40,000	80,000	120,000
ϕ', friction angle (degree)	35	40	45
R_{inter}, interface factor	0.6	0.8	1
Reinforcement			
J, stiffness (kN/m)	200	470	800
T_{ult}, ultimate tensile strength (kN/m)	30	54	80
Geometric configuration			
L/H, wall aspect ratio[b]	0.5	0.7	0.9
S_v, reinforcement vertical spacing (m)	0.2	0.4	0.6

Note:
[a] The E_{50}^{ref} and E_{oed}^{ref} relationship is in accordance with a fixed ratio of 1.33.
[b] The aspect ratios were increased to $L/H = 4.2$ to investigate the failure mode of GRS barriers in the previous section.

Table 2
Summary of failure modes and ultimate lateral capacity factors with various L/H.

Wall aspect ratio	$0.5 < L/H < 1.0$	$1.0 < L/H < 3.0$	$L/H > 0.3$
Failure type	Internal	External	Internal
Failure mode Description	Interlayer sliding at loading side and soil active failure at free-end side	Bottom sliding failure	Soil passive failure
Ultimate lateral capacity factor, N_L[a]	0.32–1.2 (=1.4–5.52K_a)	1.2–4.38 (=5.52–20.16K_a)	>4.38 (>20.16K_a)

Note:
[a] Ultimate lateral capacity factor is calculated by Eq. (1). The values in parenthesis indicate the times larger than K_a.

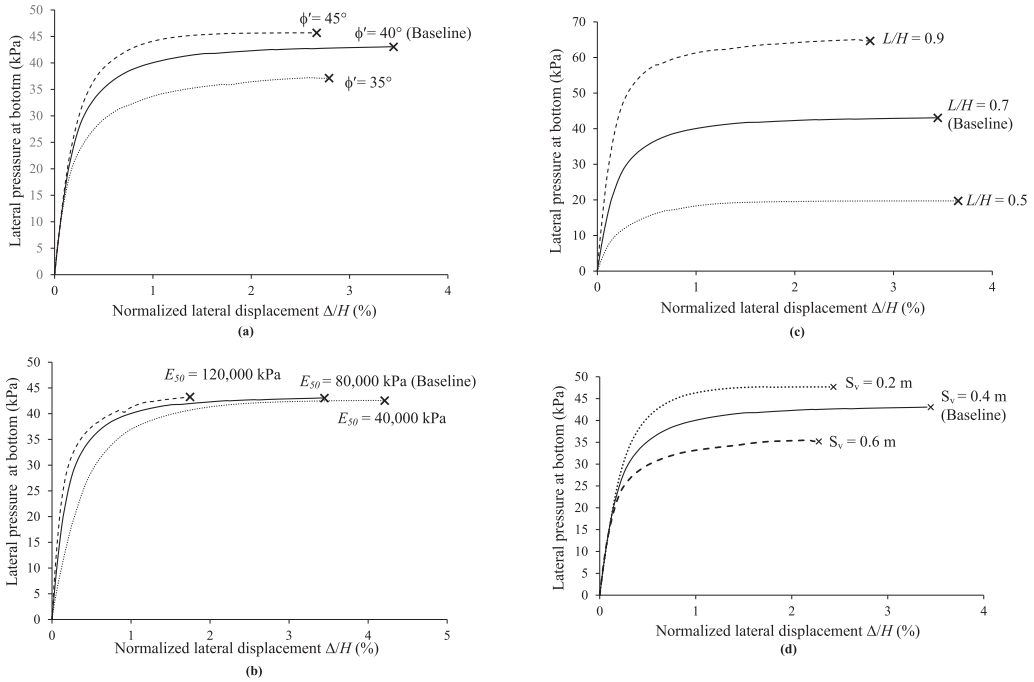

Fig. 13. Load-displacement curves for GRS barriers with various: (a) friction angles; (b) soil moduli; (c) aspect ratios; (d) reinforcement vertical spacing.

capacity of GRS barriers. Among these parameters, L/H had the greatest effect; when L/H was varied by ±30%, the ultimate lateral capacity changed by ±50%. Fig. 14 shows that the soil modulus E_{50}^{ref} and reinforcement ultimate tensile strength T_{ult} hardly have any influence on the ultimate lateral capacity of the GRS barrier. Finally, the parametric study results were applied only to the baseline case. Unlike the internal failure mode in the baseline case, failure mode changed to bottom sliding when $1.0 < L/H < 3.0$ and passive soil failure when $L/H > 3.0$. Consequently, the factors that influence the ultimate lateral capacity of the GRS barrier changed with different failure modes at different L/H ratios.

6. Hypothetical case study

A hypothetical case study of a GRS barrier against tsunamis is described in this section. Fig. 15 illustrates a 3-m GRS barrier with $L/H = 0.7$ located at 7 m (z) above sea level, and the designed maximum tsunami inundation (runup) point (R) is 10 m above the sea level. In this case study, an initial tsunami wave impact was considered. The instability caused by potential scouring at the toe of the walls and the seepage force caused by drag down in the drained phase was not examined. Miyata et al. (2015a, 2015b) studied these effects by using full-scale reinforced wall tests due to loss of foundation support and transient flooding conditions. Encouraging results were obtained from their tests. They demonstrated that the test walls performed satisfactorily under the aforementioned adverse conditions. The reserved load carrying capacity of the walls can explain favorable performance of a few GRS walls under similar conditions.

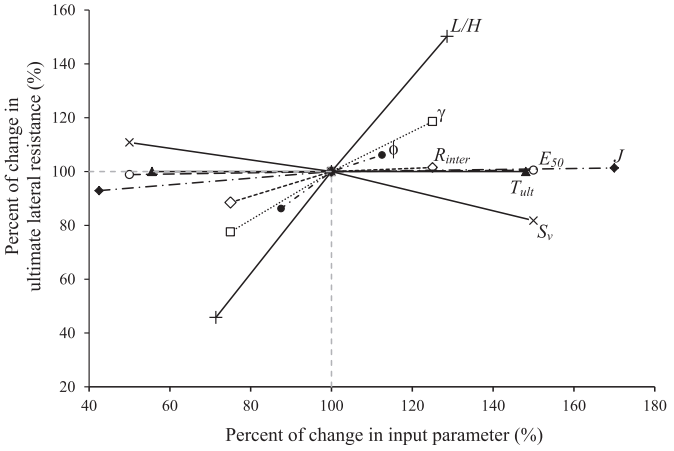

Fig. 14. Results of parametric study: Percent of change in ultimate lateral resistance vs. percent of change in input parameter.

The methods for estimating the tsunami force proposed by Yeh (2007) and adopted by FEMA (2006) were used. The tsunami force comprises hydrostatic pressure and impulsive (surge) force. The impact force by water-born debris was not considered. The hydrostatic pressure was assumed to be linearly distributed and calculated as

$$\sigma_{h,static} = \gamma_w h \tag{6}$$

where $\sigma_{h,static}$ is the hydrostatic pressure, γ_w (= 11.7 kN/m^3) is the unit weight of the mixture of seawater and sediments, and h is the water depth from the maximum tsunami inundation point. In this case, $h = H = 3$ m. Equation (6) accounts for an imbalance of hydrostatic pressure caused by a differential water depth on opposite sides of a wall.

The impulsive force is uniformly distributed and caused by the leading edge of running-up water impinging on a structure, which can be estimated as 1.5 times the hydrodynamic force, as follows:

$$F_s = 1.5F_d \tag{7}$$

where F_s is the impulsive force and F_d is the hydrodynamic force, often called the drag force. F_d can be computed as follows:

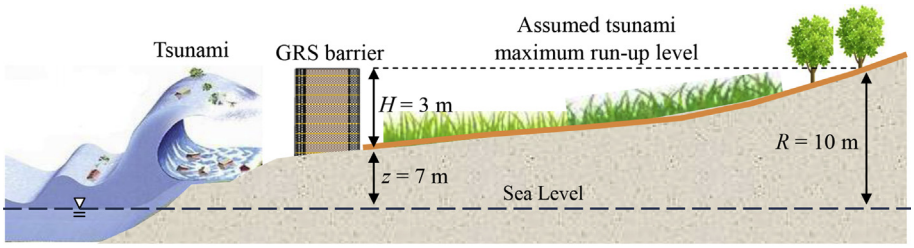

(a)

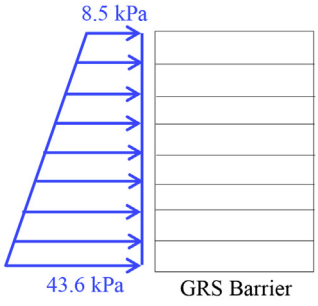

(b)

Fig. 15. Schematic illustration of the case scenario assumed in this study: (a) dimensions and location of the GRS barrier; (b) calculated total lateral force acting on the GRS barrier.

$$F_d = \frac{1}{2}\frac{\gamma_w}{g} C_d B \left(hu^2\right)_{\max} \tag{8}$$

where g is the gravity, C_d is the drag coefficient (2.0 for square or rectangular objects), B is the width of the structure (1.0 for unit width), and $(hu^2)_{\max}$ is the maximum momentum flux. Next, $(hu^2)_{\max}$ can be determined using the following equation by Yeh (2006), which is based on the exact analytical solution of the nonlinear shallow water wave theory:

$$\left(hu^2\right)_{\max} = 0.125 - 0.235\frac{z}{R} + 0.11\left(\frac{z}{R}\right)^2 \tag{9}$$

where R is the ground elevation at the maximum tsunami inundation points and z is the ground elevation of the location of interest. In this case, $R = 10$ m and $z = 7$ m (Fig. 15). By using Eqs. (6)–(9), a tsunami wave impact pressure, trapezoidally distributed with 8.5 kPa at the top and 43.6 kPa at the bottom, was applied to the GRS barrier, and stability was evaluated numerically (Fig. 15b). Note that the wall geometry, material properties, and construction procedure used in the hypothetical case study were identical to those in the baseline case (Section 3.1).

The numerical results (Fig. 16) suggested that the GRS barrier with $L/H = 0.7$ can only sustain approximately 70% of the tsunami force. The original design would fail in this hypothetical case. One viable solution is to increase L/H. As discussed previously, the ultimate lateral bearing capacity of GRS barriers can be improved by increasing L/H. The numerical results revealed that when L/H was increased to 0.9, the GRS barrier successfully sustained 100% of tsunami force. However, if the construction space is constrained because of the high cost of additional right-of-way or limited space available on the job sites, a feasible solution is to install vertical soil anchors. This approach was first proposed by Uchimura et al. (2005) for evaluating the performance of a preloaded and prestressed geogrid-reinforced soil wall as a bridge pier under vertical and horizontal loading tests. Fig. 17 shows an FE model of a GRS barrier improved with two rows of vertical soil anchors. The anchor heads are placed on a load plate on top of the wall to distribute more uniformly the vertical load on the wall. In the FE model, node-to-node spring elements with an axial stiffness of 3×10^7 kN/m and out-of-plane spacing of 2.5 m were selected to model the anchor rods, and geogrid elements with an axial stiffness of 6.5×10^5 kN/m were used to model the ground body. A 50-kN pretension force was applied to the anchors. As shown in Fig. 16, the ultimate lateral bearing capacity of the GRS barrier was significantly improved using two rows of vertical soil anchors, and 100% tsunami force was sustained by the improved design. The numerical results revealed that placing preloaded soil anchors can improve soil–reinforcement interaction and therefore effectively increase the lateral bearing capacity.

7. Conclusions

This paper presents a series of FE analyses to investigate the failure mode and lateral bearing capacity of GRS barriers subject to

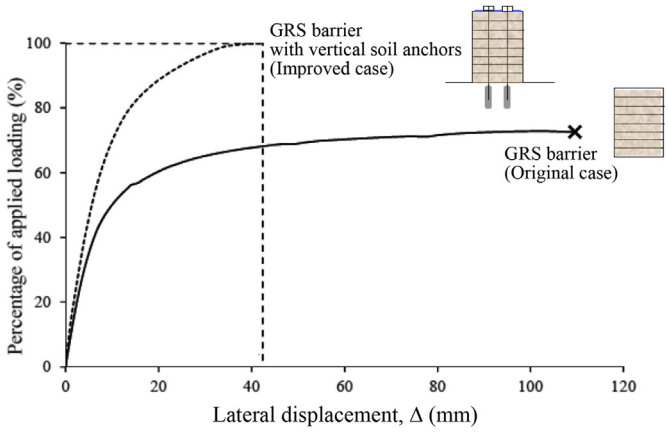

Fig. 16. Load-displacement curves for original and improved GRS barriers.

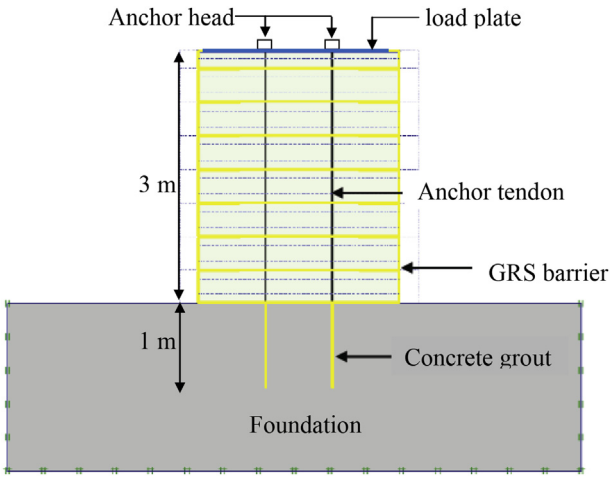

Fig. 17. FE model of the GRS barrier improved by vertical soil anchors with 50 kN preload.

lateral loadings. The FE model was verified by experimental results obtained using a large-scale test on a back-to-back GRS wall. Parametric studies and a hypothetical case study were performed and discussed. Specific conclusions and discussions are summarized as follows:

1. The FE results indicated that the failure mode and lateral bearing capacity of GRS barriers subject to lateral loadings depended largely on the aspect ratio *L/H*.
2. At $0.5 < L/H < 1.0$, GRS barriers would fail internally because of internal sliding along the soil–reinforcement interface at the loading side and active soil failure at the opposite side (the side without external loads). The mobilized reinforcement tensile force concentrated on the side subject to external loads, particularly in reinforcement layers 1–4 located from bottom to mid-height of the wall, was attributed to the active soil failure caused by an increase in the vertical stress on this side.
3. For a GRS barrier with $0.5 < L/H < 0.7$, the internal soil failure obtained using FE method differed from that of a rigid body assumed for reinforced soil mass in design guidelines.
4. At $1.0 < L/H < 3.0$, failure would occur along the foundation–reinforcement interface, and the ultimate lateral bearing capacity agreed well with that obtained by theoretical sliding equation.
5. At $L/H > 3.0$, soil behind wall face would fail in a passive condition, and the ultimate lateral bearing capacity can be described using the Rankine's passive lateral earth pressure theory.
6. The ultimate lateral bearing capacity of GRS barriers increased with an increase in *L/H*. The ultimate lateral capacity factor N_L was 1.4–20.1 times K_a for $L/H = 0.5$–3.0.
7. The parametric study reveals that the aspect ratio *L/H*, backfill friction angle ϕ, unit weight γ, and reinforcement vertical spacing S_v all have considerable influence on lateral bearing capacity of GRS barriers at baseline case.
8. For the hypothetical GRS barrier examined in this study, the lateral bearing capacity was significantly improved by using two rows of vertical preloaded soil anchors.

The results of plane strain two-dimensional (2D) FE analyses presented in this paper represent situations where massive lateral loadings, such as those derived from tsunamis, debris flows, and avalanches. For situations where lateral loadings acting only over a small area, such as the local impact from rockfalls, 2D FE plane strain analysis would give conservative results, and three-dimensional FE analysis is recommended for such situations. In addition, this study focused on a vertical GRS barrier with continuous reinforcement. The effect of wall configuration (facings with different inclination angles) and reinforcement layout (with or without connection of two sides of reinforcement at the middle) needs further evaluation. Finally, this study addressed only the results of FE analyses of GRS barriers placed on a rigid foundation. The results presented in this paper is applicable to firm foundation of which settlement is negligible, and where toe erosion or scouring of the toe is not a concern. The adverse effects of soft foundation and water-wave-induced toe erosion or scouring on the stability of GRS structures require further investigation.

Acknowledgments

The financial supports for this study were provided by the Ministry of Science and Technology of Taiwan to the first author for short-term research aboard project (MOST104-2918-I-011-006) and to the second author for his sabbatical visit to the National Taiwan University (NSC-101-2811-E-002-014) and the National Taiwan University of Science and Technology.

Notations

Basic SI units are given in parentheses

B	width of structure (m)
c'	cohesion (kPa)
c_a	reinforcement-foundation interface cohesion (kPa)
C_d	drag coefficient (dimensionless)
E	Young's modulus (kPa)
E_{50}^{ref}	secant modulus (kPa)
E_{oed}^{ref}	tangent modulus for primary oedometer loading (kPa)
E_{ur}^{ref}	unloading-reloading modulus (kPa)
F_d	hydrodynamic force (kN/m)
F_s	impulsive force (kN/m)
g	gravity (m/s^2)
H	wall height (m)
$(hu^2)_{max}$	Maximum momentum flux of tsunami ($m^3/^{s2}$)
h	water depth from the maximum tsunami inundation point (m)
I	moment of inertia (m^4)
J	reinforcement stiffness (kN/m)
K_a	active earth pressure coefficient (dimensionless)
K_p	passive earth pressure coefficient (dimensionless)
L	wall width (m)
L/H	wall aspect ratio (dimensionless)
M	bending moment induced by lateral loading (kN-m)
m	modulus exponent (dimensionless)
N_L	ultimate lateral capacity factor (dimensionless)
P_u	total lateral resistance per unit length (kN/m)
R	tsunami run-up level (m)
R_{inter}	reduction factor for interface (dimensionless)
R_f	failure ratio (dimensionless)
S_v	vertical spacing between reinforcement layers (m)
T_{ult}	ultimate tensile strength (kN/m)
W	self-weight of GRS barrier per unit length (kN/m)
x	horizontal distance from loading side (m)
x_1	horizontal distance from neutral plane (m)
x/L	normalized horizontal distance (dimensionless)
y	elevation from wall bottom (m)
y/H	normalized elevation (dimensionless)

z	elevation above sea level (m)
Δ	maximum lateral displacement (m)
Δ/H	normalized lateral displacement (%)
δ	reinforcement-foundation interface friction angle (degree)
γ	unit weight of backfill soil or facing block (kN/m^3)
γ_w	unit weight of seawater and sediment mixture (kN/m^3)
σ_3	confining pressure (kPa)
$\sigma_{h@bottom}$	applied ultimate lateral pressure at bottom (kPa)
$\sigma_{h,\ static}$	Hydrostatic pressure (kPa)
$\Delta\sigma_v$	vertical stress increment (kPa)
ν	Poisson's ratio of facing block (dimensionless)
ν_{ur}	Poisson's ratio for unloading-reloading (dimensionless)
ϕ	peak friction angle (degree)
ψ	angle of dilatancy (degree)
τ_{max}	maximum interface shear strength (kN/m^2)
$\tau_{mobilized}$	mobilized interface shear stress (kN/m^2)
τ_{rel}	interface shear stress mobilization ratio (dimensionless)

References

Anubhav, S., Basudhar, P.K., 2011. Numerical modelling of surface strip footings resting on double-faced wrap-around vertical reinforced soil walls. Geosynth. Int. 18 (1), 21–34.

ASTM D4595. Standard Test Method for Tensile Properties of Geotextiles by the Wide-width Strip Method. American Society for Testing and Materials, West Conshohocken, PA, USA.

Bathrust, R.J., Hatami, K., 1998. Seismic response analysis of a geosynthetic-reinforced soil retaining wall. Geosynth. Int. 5 (1–2), 127–166.

Berg, R., Christopher, B.R., Samtani, N., 2009. Design of Mechanically Stabilized Earth Walls and Reinforced Soil Slopes. Report No. FHWA-NHI-10–024, I and II. National Highway Institute, Federal Highway Administration, Washington, D.C. March.

Boyle, S.R., Gallagher, M., Holtz, R.D., 1996. Influence of strain rate, specimen length and confinement on measured geotextile properties. Geosynth. Int. 3 (2), 205–225.

Brandl, H., 2011. Geosynthetics applications for the mitigation of natural disasters and for environmental protection. Geosynth. Int. 18 (6), 340–390.

Carotti, A., Peila, D., Castiglia, C., Rimoldi, P., 2000. Mathematical modelling of geogrid reinforced embankments subject to high energy rock impact. Proceedings of the 2nd European Geosynthetics Conference and Exhibition — Eurogeo II, Bologna, Italy, 305–310.

Choudhury, D., Ahmad, 2007. Design of waterfront retaining wall for the passive case under earthquake and tsunami. Appl. Ocean Res. 29, 37–44.

Cristelo, N., Felix, C., Lopes, M.L., Dias, M., 2016. Monitoring and numerical modelling of an instrumented mechanically stabilized earth wall. Geosynth. Int. 23 (1), 48–61.

Damians, I.P., Bathurst, R.J., Josa, A., Lloret, A., 2014. Numerical analysis of an instrumented steel-reinforced soil wall. Int. J. Geomechanics 15 (1), 1–15.

Ehrlich, M., Mirmoradi, 2012. Evaluation of the effect of compaction on the behavior of geosynthetic-reinforced soil walls. Geotext. Geomembranes 34, 108–115.

Ehrlich, M., Mirmoradi, S.H., Saramago, R.P., 2013. Evaluation of the effects of facing stiffness and toe resistance on the behavior of GRS walls. Geotext. Geomembranes 40, 28–36.

El-Emam, M., Bathrust, R.J., 2007. Influence of reinforcement parameters on the seismic response of reduced-scale reinforced soil retaining walls. Geotext. Geomembranes 25 (1), 33–49.

El-Emam, M.M., Bathurst, R.J., 2004. Experimental design, instrumentation and interpretation of reinforced soil wall response using a shaking table. Int. J. Phys. Model. Geotechnics 4, 13–32.

El-Emam, M.M., Bathurst, R.J., 2005. Facing contribution to seismic response of reduced-scale reinforced Soil Walls. Geosynth. Int. 12 (5), 215–238.

Elias, V., Christopher, B.R., Berg, R.R., 2001. Mechanically Stabilized Earth Walls and Reinforced Soil Slopes Design and Construction Guidelines. Report No. FHWA-NHI-00–043. National Highway Institute, Federal Highway Administration, Washington, D.C.

FEMA, 2006. Guidelines for Design of Structures for Vertical Evacuation from Tsunamis. Report No. 361. Federal Emergency Management Agency, Washington, D.C.

Fowze, J.S.M., Bergado, D.T., Soealump, S., Voottipreux, P., Dechasakulsom, M., 2012. Rain-triggered landslide hazards and mitigation measures in Thailand: from research to practice. Geotext. Geomembranes 30, 50–64.

Guler, E., Hamderi, M., Demirkan, M.M., 2007. Numerical analysis of reinforced soil-retaining wall structures with cohesive and granular backfills. Geosynth. Int. 14 (6), 330–345.

Han, J., Leshchinsky, D., 2010. Stability analysis of back–to–back MSE walls. Geotext. Geomembranes 28 (3), 262–267.

Hatami, K., Bathurst, R.J., 2005. Development and verification of a numerical model for the analysis of geosynthetic-reinforced soil segmental walls under working stress conditions. Can. Geotechnical J. 42 (4), 1066–1085.

Hong, Y.-S., Wu, C.-S., 2013. The performance of a sand column internally reinforced with horizontal reinforcement layers. Geotext. Geomembranes 41, 36–49.

Huang, C.-C., Horng, J.-C., Chueh, S.-Y., Chiou, J.-S., Chen, C.-H., 2010. Dynamic behavior of reinforced slopes: horizontal acceleration response. Geosynth. Int. 17 (4), 207–219.

Huang, C.-C., Horng, J.-C., Chueh, S.-Y., Chiou, J.-S., Chen, C.-H., 2011. Dynamic behavior of reinforced slopes: horizontal displacement response. Geotext. Geomembranes 29, 257–267.

Japanese Geotechnical Society, 2011. Geo-hazards During Earthquakes and Mitigation Measures-lessons and Recommendations from the 2011 Great East Japan Earthquake, p. 84.

Kim, K.-M., Briaud, J.-L., Bligh, R., Abu-Odeh, A., 2010. Full-scale impact test of four traffic barriers on top of an instrumented MSE wall. J. Geotechnical Geoenvironmental Eng. ASCE 136 (3), 431–438.

Koseki, Shibuya, S., 2014. Mitigation of disasters by earthquakes, tsunamis, and rains by means of Geosynthetic-reinforced soil retaining walls and embankments. Transp. Infrastruct. Geotechnol. 2 (1), 231–261.

Krishna, A.M., Latha, G.M., 2007. Seismic response of wrap-faced reinforced soil-retaining wall models using shaking table tests. Geosynth. Int. 14 (6), 355–364.

Kuwano, J., Miyata, Y., Koseki, J., 2012. Performance of reinforced soil walls during the 2011 Tohoku earthquake. Geosynth. Int. 21 (3), 179–196.

Lambert, S., Bourrier, F., 2013. Design of rockfall protection embankments: a review. Eng. Geol. 154, 77–88.

Latha, G.M., Krishna, A.M., 2008. Seismic response of reinforced soil retaining wall models: influence of backfill relative density. Geotext. Geomembranes 26, 335–349.

Ling, H.I., Mohri, Y., Leshchinsky, D., Burke, C., Matsushima, K., Liu, H.-B., 2005. Large-scale shaking table tests on modular-block reinforced soil retaining walls. J. Geotechnical Geoenvironmental Eng. 131 (4), 465–476.

Liu, H., Wang, X., Song, E., 2010. Centrifuge testing of segmental geosynthetic-reinforced soil retaining walls subject to modest seismic loading. GeoFlorida 2010 Adv. Analysis Model. Des. 2992–2998.

Matsuo, O., Tsutsumi, T., Yokoyama, K., Saito, Y., 1998. Shaking table tests and analysis of geosynthetic-reinforced soil retaining walls. Geosynth. Int. 5 (1–2), 97–126.

Mirmoradi, S.H., Ehrlich, M., 2014. Numerical evaluation of the behavior of GRS walls with segmental block facing under working stress conditions. J. Geotechnical Geoenvironmental Eng. 141 (3), 1–8.

Miyata, Y., Bathurst, R.J., Miyatake, H., 2015a. Performance of three geogrid-reinforced soil walls before and after foundation failure. Geosynth. Int. 22 (4), 311–326.

Miyata, Y., Bathurst, R.J., Otani, Y., Ohta, H., Miyatake, H., 2015b. Influence of transient flooding on steel strip reinforced soil walls. Soils Found. 55 (4), 881–894.

Murali, A.K., Madhavi, G.L., 2012. Modeling the dynamic response of wrap-faced reinforced soil retaining walls. Int. J. Geomechanics 12 (4), 439–450.

Nicks, J.E., Esmaili, D., Adams, M.T., 2016. Deformations of geosynthetic reinforced soil under bridge service loads. Geotext. Geomembranes 44, 641–653.

Nova-Roessig, L., Sitar, N., 2006. Centrifuge model studies of the seismic response of reinforced soil slopes. J. Geotechnical Geoenvironmental Eng. 13 (3), 388–400.

Peila, D., Oggeri, C., Castiglia, C., 2007. Ground reinforced embankments for rockfall protection: design and evaluation of full scale tests. Landslides 4, 255–265.

PLAXIS, 2005. PLAXIS Finite Element Code for Soil and Rock Analyses. Version 8.2, P.O. Box 572, 2600 AN Delft, The Netherlands.

Recio-Molina, J., Yasuhara, K., 2005. Stability of modified geotextile wrap around revetments for coastal protection. Geosynth. Int. 12 (5), 260–268.

Ren, F., Zhang, F., Xu, C., Wang, G., 2016. Seismic evaluation of reinforced-soil segmental retaining walls. Geotext. Geomembranes 44, 604–614.

Ronco, C., Oggeri, C., Peila, D., 2009. Design of reinforced ground embankments used for rockfall protection. Nat. Hazards Earth Syst. Sci. 9, 1189–1199.

Santos, E.C.G., Palmeira, E.M., Bathurst, R.J., 2013. Behaviour of a geogrid reinforced wall built with recycled construction and demolition waste backfill on a collapsible foundation. Geotext. Geomembranes 39, 9–19.

Santos, E.C.G., Palmeira, E.M., Bathurst, R.J., 2014. Performance of two geosynthetic reinforced walls with recycled construction waste backfill and constructed on collapsible ground. Geosynth. Int. 24 (4), 256–269.

Soude, M., Chevalier, B., Grediac, M., Talon, A., Gourves, R., 2013. Experimental and numerical investigation of the response of geocell reinforced walls to horizontal localized impact. Geotext. Geomembranes 39, 39–50.

Tatsuoka, F., Koseki, J., Tateyama, M., 1995. Performance of geogrid-reinforced soil retaining walls during the Great Hanshin-Awaji earthquake, January 17, 1995. In: Proc., the First International Conference on Earthquake Geotechnical Engineering, IS Tokyo '95, pp. 55–62.

Tuan, C., 2013. Ground shock resistance of mechanically stabilized earth walls. Int. J. Geomechanics ASCE 14 (3), 06014003.

Uchimura, T., Tamura, Y., Tateyama, M., Tanaka, I., Tatsuoka, F., 2005. Vertical and horizontal loading tests on full-scale preloaded and prestressed geogrid-reinforced soil structures. Soils Found. 45 (6), 75–88.

Vahedifard, F., Leshchinsky, D., Meehan, C.L., 2013. Displacement-based internal design of geosynthetic-reinforced earth structures subjected to seismic loading conditions. Géotechnique 63 (6), 451–462.

Walz, B., 1982. Bodenmechanische Modelltechnik als Mittel zur Bemessung von Grundbauwerken. Forschungs- und Arbeitsberichte aus den Bereichen Grundbau, Bodenmechanik und unterirdisches Bauen, Bergische Universität – GH Wuppertal, Germany, No. 1 (in German).

Wu, J.T.H., Pham, T.Q., 2013. Load-carrying capacity and required reinforcement strength of closely-spaced soil-geosynthetic composites. J. Geotechnical Geoenvironmental Eng. ASCE 139 (9), 1468–1476.

Wu, J.T.H., Ma, C.Y., Pham, T.Q., Adams, M.T., 2011. Required minimum reinforcement stiffness and strength in geosynthetic-reinforced soil (GRS) walls and abutments. Int. J. Geotechnical Eng. 5 (4), 395–404.

Wu, J.T.H., Yang, K.-H., Mohamed, S., Pham, T., Chen, R.-H., 2014. Suppression of soil dilation-A reinforcing mechanism of soil-geosynthetic composites. Transp. Infrastruct. Geotechnol. 1 (1), 68–82.

Yasuhara, K., Recio-Molina, J., 2007. Geosynthetic-wrap around revetments for shore protection. Geotext. Geomembranes 25, 221–232.

Yeh, H., 2006. Maximum fluid forces in the tsunami runup zone. J. Waterw. Port, Coast. Ocean Eng. ASCE 132, 496–500.

Yeh, H., 2007. Design tsunami forces for onshore structures. J. Disaster Res. 2 (6), 531–536.